Journal of Colloid and Interface Science 460 (2015) 36–46

Contents lists available at ScienceDirect

Journal of Colloid and Interface Science

journal homepage: www.elsevier.com/locate/jcis

The impact of particle size on the adsorption of citrate to hematite

Matthew R. Noerpel, John J. Lenhart *

Department of Civil, Environmental, and Geodetic Engineering, The Ohio State University, Columbus, OH 43210, USA

GRAPHICAL ABSTRACT

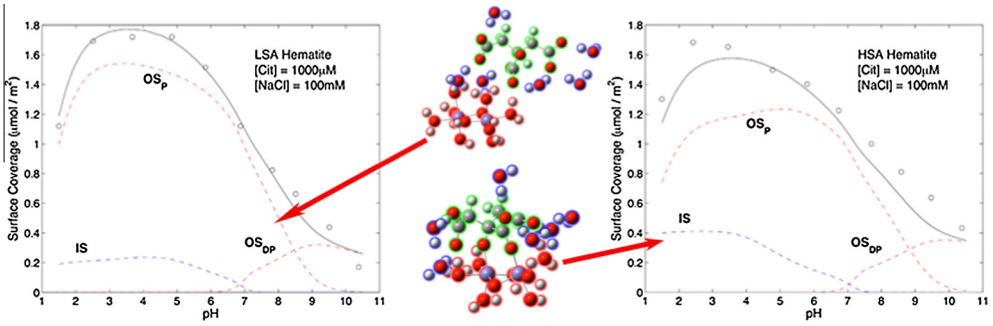

ARTICLE INFO

Article history:
Received 19 June 2015
Revised 13 August 2015
Accepted 14 August 2015
Available online 15 August 2015

Keywords:
Hematite
Citrate
Adsorption
FTIR spectroscopy

ABSTRACT

We investigated the adsorption of citric acid on the surface of two different sized hematite nanoparticles using batch adsorption experiments, Fourier-transform infrared spectroscopy, surface complexation modeling and computational molecular modeling. Citrate adsorption reached a maximum between pH approximately 2.5 and 5.5 and declined as the pH was increased or decreased from that range. At high surface loading conditions, the dominant adsorbed citrate structure was outer-sphere in nature with a protonation state that varied with pH. At low pH, there was also evidence of an inner-sphere complex consistent with a binuclear, bidentate structure where the hydroxyl group was deprotonated and played an active role in the adsorption. An inner-sphere complex was also detected at low citrate surface loading conditions. Surface-area normalized surface coverages were similar for both sizes of hematite, however, the inner sphere complex appeared to be slightly more prevalent on the smaller hematite. Based on these structures, a triple layer surface complexation model comprised of two outer-sphere complexes and one inner-sphere complex was used to describe the adsorption data for both hematite sizes across a range of solution conditions with a single set of surface area dependent equilibrium constants.

1. Introduction

Organic acid interactions with metal oxide surfaces are a ubiquitous presence in natural soils and play an important role in many biological and geochemical processes [1]. When bound to an oxide surface, organic acids can alter the surface properties of the underlying mineral, which modifies its solubility and interactions with other solutes [2]. Organic acids also influence particle fate in the environment by altering the steric and electrostatic interactions that control aggregation and transport [2–4]. In addition to the effect organic acids have on particle surface reactivity they also bind metals in solution, either preventing or enhancing the metal's adsorption [5] and thus organic acids can impact metal transport through soil [4,6–8]. Therefore, understanding the conditions that control organic acid adsorption to metal oxide surfaces and the coordination modes of those acids will lead to a better understanding of metal transport in contaminated soils.

* Corresponding author.
E-mail address: lenhart.49@osu.edu (J.J. Lenhart).

http://dx.doi.org/10.1016/j.jcis.2015.08.028
0021-9797/

There are a wide variety of organic acids present in natural soils that can bind to metal oxides. Humic and fulvic acids are among the most prevalent and they are comprised of large polyelectrolytic, polyfunctional acids heterogeneous in size and structure [9,10]. While these humic substances are ubiquitous in soils and play an important role in soil chemistry, elucidating their fundamental adsorption mechanisms remains a challenge [11]. One alternative is to instead use low molecular weight organic acids of known structure that share common functional groups (e.g., carboxylic acid) with heterogeneous humic substances [10,12]. In this study, citric acid was used as a representative organic acid due to its prevalence in the environment and functional group similarities with humic substances [13]. Citric acid is used by plants and microorganisms as a metal chelator in iron and phosphate deprived soils to more efficiently extract the iron and phosphate necessary for growth [14,15] and in low pH soils to prevent aluminum toxicity [16]. Citric acid has three carboxylic acid functional groups, with intrinsic pK_as of 3.13, 4.76, and 6.40 [17], and one hydroxyl group that deprotonates at pH values estimated to be between 11 and 14.4 [18]. The pK value for the hydroxyl group is out of the range of this study; however, that does not preclude it from deprotonating and playing an active role in the adsorption process as it does when complexing aluminum or gallium [19].

Hematite (α-Fe_2O_3) is thermodynamically very stable and it is a common end result of the transformation of other less stable iron oxides [20]. As such it is commonly found in natural soils, especially older soils, in both nanoscale and larger forms [20]. Hematite readily binds organic and inorganic species and in a colloidal form it is implicated in the larger than anticipated transport of heavy metals through sediment and subsurface systems [21,22]. The different crystalline faces of hematite display varying reactivity and available binding sites. For example, the (001) face, considered the most common face, has a net neutral surface charge between pH 2 and 10 [23] while the pH_{pzc} of whole hematite particles is reported to be between 8.5 and 9.5 [24,25]. This lack of surface charge in the environmentally relevant pH range results in the (001) surface being less reactive than other common surfaces and makes aggregation and adsorption processes on the (001) surface less dependent on pH [23].

The size of the hematite particles is expected to play an important role in adsorption processes as the relative abundance of the different crystalline faces and their associated binding sites may change with particle size [26,27]. For example, Madden et al. [26] determined that the affinity of Cu(II) to hematite changed with particle size as the smaller hematite had a higher proportion of irregular octahedral binding sites preferred by Cu(II). This occurred even though both particles exhibited the same pseudo hexagonal morphology. Similar results were also demonstrated with the iron hydroxide goethite, which displays a better defined crystal morphology than does hematite [27]. To isolate the role of different crystalline faces of goethite, atomic force microscopy was used to determine the (001) face made up 70% of the surface of larger crystals versus 30% of that for smaller crystals [27]. Thus, the adsorption capacity of the goethite crystals will not scale directly with available surface area if the adsorbate has a preference for sites in the (001) face [27]. In this study we use two different sizes of hematite to investigate the effect of particle size, and by inference, crystal face distribution on the adsorption of citrate to hematite.

In comparison to the extensive literature of citrate adsorption on goethite and other oxides, details of citrate adsorption on hematite are limited. For example, Zhang et al. [28] used macroscopic adsorption and iron dissolution experiments to conclude that citrate adsorbed as both doubly and triply deprotonated species. As part of the same study, Kallay and Matijevic [29] used zeta potential measurements and surface complexation modeling to determine that citrate is bound directly to the hematite surface via a bidentate structure and that both singly protonated and fully deprotonated citrate surface species exist. Additional research has been performed on the iron oxyhydroxide, goethite, and the isostructural aluminum oxide, corundum. For example, Hidber et al. [30] used a variety of methods, including Fourier transform infrared (FTIR) spectroscopy, to investigate citric acid adsorption on corundum (α-Al_2O_3). They reported citrate adsorbs in an inner sphere manner, but not with all three carboxyl groups. Hidber et al. [30] did not find direct evidence for the involvement of the hydroxyl group in citrate binding but assume it is involved due to differences between its adsorption and that for tricarballylate, which differs from citrate by lacking the additional hydroxyl group. Results with goethite are more extensive, with early investigators primarily invoking inner-sphere surface complex modes, such as one involving the citrate ion adsorbing in a triply coordinated manner using all three carboxyl groups [31]. More recent results have increasingly found outer-sphere adsorption modes, with Lackovic et al. [32] indicating inner-sphere complexation at low- to mid-pH gives way to outer-sphere complexation at elevated pH. This interpretation was based on FTIR spectroscopy coupled to batch adsorption and goethite dissolution experiments [32]. Lindegren et al. [33] reported finding multiple inner- and outer-sphere surface structures using 2-D correlation infrared spectroscopy, including two previously unreported structures. These new structures included a protonated outer-sphere complex at low pH and an inner-sphere structure at high pH where the hydroxyl group deprotonated and played an active role in the adsorption process. Most recently, Yeasmin et al. [34] used batch adsorption experiments with ^{14}C-labeled organic acids and infrared spectroscopy and came to a similar conclusion as Lindegren et al. that citrate adsorbs on goethite (and ferrihydrate) as mono- and bidentate inner sphere complexes as well as outer-sphere complexes. Unfortunately, they did not further specify the structure of the adsorbed citrate.

The main method of investigation in this study to determine the structure of adsorbed citrate onto hematite was Attenuated Total Reflectance FTIR (ATR-FTIR) spectroscopy. As the different structural features of the citrate molecule absorb infrared energy at specific frequencies, the changes in frequency and magnitude of that absorption can indicate changes in the coordination of the molecule [32,33,35]. These experimentally determined infrared spectra were compared with those produced through computational methods. Calculating the theoretical infrared spectra of different potential structures allows us to assign specific vibrations to the peaks visible in the experimental FTIR spectra and compare the experimental results of the adsorbed structure to those generated theoretically based upon different potential structures [35]. Based on these constraints, a surface complexation model was derived based on the Triple Layer Model of hematite developed by Hwang and Lenhart [24] and utilized to simulate the experimental adsorption data. Our results suggest that citrate adsorbs predominantly as an outer-sphere complex on both sizes of hematite studied, with a minor addition of a bidentate inner-sphere complex that adsorbs preferentially with respect to the outer-sphere complex, but in lower concentrations due to a limited number of available surface sites. The smaller hematite particles allowed for more inner sphere adsorption suggesting it carried a greater proportion of sites that prefer to directly bind citrate.

2. Materials and methods

2.1. Hematite synthesis and characterization

Two sizes of hematite were synthesized and used in this research. The first, with a nominal 10 nm diameter was synthesized

following methods in Madden et al. [26] by slowly dripping 50 mL of a 1 M solution of $Fe(NO_3)_3$ into 625 mL of boiling Millipore water. The solution was allowed to cool gradually overnight before being cleaned. The second, with an average diameter of 50 nm, was synthesized through a forced hydrolysis method using ferric chloride as the iron source following the methods of Matijevic and Scheiner [36] and Penners and Koopal [37], with minor modifications [38]. Sufficient ferric chloride was added to 0.004 M HCl to create a 50 mL 0.8 M $FeCl_3$ solution. This solution was filtered through a 0.22 μm PVDF filter and added to 1950 mL of 0.004 M HCl preheated to 98 °C. This suspension was aged at 98 °C for 3 days before being rapidly cooled and cleaned. Both hematite suspensions were concentrated by adding solid NaOH to raise the pH leading to particle aggregation and settling. The concentrated hematite solids were collected and transferred to 8–10 kDa cellulose ester dialysis tubing (Spectrum Labs) where they were dialysed against Millipore water for several days. The dialysis water was changed twice daily until the dialysate conductivity approached that for deionized water. The suspensions were subsequently dialysed against a 1 mM $HClO_4$ solution for 24 h. Multiple batches were made and combined to create stock solutions. For hematite synthesis and all following experiments, deionized water used with a resistivity of 18.2 μS/cm was supplied using a Millipore Milli-Q Plus system. All reagents were ACS grade or higher and the glassware was cleaned using a 5% nitric acid bath followed by repeated rinsing in deionized water. The hematite particle samples were verified as crystalline hematite using X-ray diffraction (either a Scintag Pad V or Rigaku SmartLab). Particle size and morphology were determined using a Tecnai BioTwin TEM (see Fig. S1 in the Supporting Information). To image the particles, an aliquot of the stock hematite solution was diluted in deionized water and a drop was placed on wax paper. A copper carbon formvar TEM grid was placed on the drop and allowed to rest for ~20 s before wicking the solution off of the grid and drying the sample under a nitrogen stream. Surface area was measured with gas adsorption using a Micromeritics Flowsorb II 2300 BET instrument. The 10 nm particles had a BET surface area of 99 m^2/g and the 50 nm diameter hematite had a surface area of 35 m^2/g. Hereafter these particles are referred to as high and low surface area hematite (HSA and LSA), respectively.

2.2. Batch adsorption protocol

Samples of the hematite stock solutions were diluted to 10 g/L in 1 mM HCl and purged overnight using humidified nitrogen gas to remove carbon dioxide. Aliquots of the CO_2-free hematite were transferred to 50 mL polycarbonate centrifuge tubes. The appropriate amount of citric acid, NaCl and either HCl or NaOH were added, under a stream of humidified nitrogen gas, to achieve the desired acid concentration, background electrolyte concentration (0.1 M unless otherwise mentioned) and pH with a 5 g/L hematite concentration. While the type of background electrolyte can impact adsorption processes [39], NaCl was chosen because Cl^- is not infrared active, unlike other common electrolyte anions, NO_3^- and ClO_4^-. All solutions were made using CO_2-free deionized water. Although Zhang et al. [28] reported citrate adsorption was complete within 5 min, the sample tubes were allowed to equilibrate on an end-over-end rotator for 48 h to ensure both adsorption and coordination equilibrium were reached. This equilibration process was conducted in the dark to avoid light-catalyzed side reactions [40,41]. After equilibration, the final pH of the samples was measured and the samples were centrifuged for 30 min at 12,000 rpm. The supernatant was analyzed for free citrate using a Dionex ICS-2100 ion chromatography system immediately after centrifugation. Dissolved iron was measured using an inductively coupled plasma – atomic emission spectrometer (Varian Vista AX CCD-Simultaneous ICP-AES). Minimal iron was found at pH 1.5 and none was measured at higher pH values, which was in agreement with previously published studies [28,42].

2.3. ATR-FTIR spectroscopy

ATR-FTIR spectroscopy was performed with a Thermo Nicolet Nexus 670 spectrometer using a duraSampl IR 9 bounce diamond coated ATR cell. The empty cell was used for the background spectra and a new background was collected before each sample. All sample and background spectra were collected by averaging a minimum of 256 scans, at a resolution of 4 cm^{-1}, in Nicolet's OMNIC software (v. 8). Reference spectra of known structures were collected to compare to the sorbed citrate spectra. Citrate spectra in the NaCl background electrolyte were collected across a range of pH values to determine the baseline position and pH-dependence of the important citrate and citric acid IR-active groups. Ferric citrate spectra, created using a mixture of 0.2 M sodium citrate and 0.07 M $FeCl_3$, were also collected across a range of pH values to serve as a model for inner sphere complexation. A 0.1 M NaCl solution was subtracted from all of the reference spectra to remove the influence of the H—O—H bending motion from water.

Sorbed citrate spectra were measured on the wet paste collected after centrifugal separation of the hematite at the conclusion of the batch sorption experiments. The paste was applied to the surface of the ATR crystal and covered with reserved supernatant and a crystal cap to prevent dehydration of the paste during measurement. In order to remove the dominant H—O—H bending vibration of water (at ~1635 cm^{-1}), a spectrum from a hematite-only wet paste was subtracted from the citrate coated hematite sample spectra following the approach described in Hwang et al. [35] and similar to the methods of Kubicki et al. [43,44]. Subtracting the hematite wet paste spectrum rather than plain water or a supernatant spectrum was necessary to account for changes in the H—O—H intensity due to the physisorbed water at the surface of the hematite [1].

2.4. Molecular modeling

Using a computational method to calculate theoretical vibrational spectra allowed us to test various proposed surface structures implied from the experimental IR spectra. A variety of plausible structures, both inner- and outer-sphere, were tested. One of the challenges in working with hematite is the difficulty in identifying specific crystalline faces [45], making it challenging to perform theoretical analyses using a slab model. Thus, the hematite surface was modeled using a small cluster comprised of one or two iron atoms as this approach has been shown to perform well vs. periodic slab models [46]. The makeup of the two types of clusters used were $Fe(OH_2)_6$ for mononuclear complexes and $Fe_2(OH)_4(OH_2)_6$ for binuclear complexes [35,47]. In the case of the inner sphere complexes, the carboxylic groups from the citrate displaced OH_2 groups. Both the aqueous and adsorbed citrate structures were optimized using density function theory (DFT) at the B3LYP [48–50] level of theory with 6-31+G(d) basis set for all atoms [51]. This same level of theory was used for the vibrational calculations. Solvation effects were taken into account by using the Integrated Equation Formalism – Polarizable Continuum Model (IEF–PCM) for water [52] as well as explicit water molecules [35]. Calculations were performed with and without explicit water molecules. The addition of explicit water molecules was found to give superior results for the citrate only spectra, so only these results are reported. All calculations were performed using Gaussian 09 [53] at the Ohio Supercomputer Center. Optimized structures are presented in Fig. S2.

2.5. Surface complexation modeling

Surface complexation modeling was applied to simulate the results of the batch adsorption experiments to further validate the structures taken from the infrared and molecular modeling calculations by extending them to fit macroscopic trends in adsorption across a range in solution conditions. We chose to utilize the triple layer model (TLM) because it possesses the complexity necessary to simulate dual-mode adsorption, which previous research for citrate adsorption on goethite suggests is possible [32–34], and because TLM parameters for hematite used in this research were determined by Hwang and Lenhart [24]. These model parameters are summarized in Table 1. All fits were done in FITEQL v. 4. [54]. The goodness of fit was determined using a weighted sum of squares/degrees of freedom (WSOS/DF) as determined by FITEQL. All of the fits utilized a relative error of 0.1 for pH and an absolute error for citrate of 0.01 * the total citrate concentration [55,56].

3. Results and discussion

3.1. Adsorption data

The adsorption envelope for citrate on hematite (Fig. 1) agrees with the expected adsorption of a multiprotic organic acid on an iron oxide surface with a broad adsorption maximum in the acidic to near neutral pH range and declining adsorption with increasing pH [17]. As the pH increases, the charge on the citrate molecule changes from neutral below the first pK_a of 3.13 to negative three above the final pK_a of 6.40. The surface charge of the hematite also changes with pH, going from positive in the acidic pH region to zero at the pH_{pzc} around pH 9 [24] and then negative at higher pH values. The adsorption data shown for the different sized particles reflect the concentrations of citric acid necessary to saturate the particle surface. While the high surface area hematite adsorbed over twice as much citrate when normalized to mass (Fig. 1a), the maximum adsorption for the two particles was very similar when normalized to surface area (Fig. 1b). The envelope shape, however, was subtly different for the two hematite types. For example, the HSA hematite featured a sharp adsorption maximum centered at pH 2.5 while the LSA hematite exhibited a flatter peak between pH 2.5 and 5.5. At elevated pH values, the pH dependence of citrate adsorption to the HSA hematite was lower than that for the LSA hematite. The position of the adsorption edge for LSA and HSA coincided quite closely. This was in contrast to Madden et al. [26] observing that the adsorption edge for Cu(II) shifted down 0.6 pH units on HSA hematite versus LSA hematite.

The change in the surface coverage of citrate on LSA hematite was evaluated at 0, 100, and 500 mM NaCl (Fig. 2). At pH 2, an increase in NaCl from 0 to 500 mM reduced adsorption as the surface coverage of citrate at 500 mM NaCl was approximately 70% of that observed in the system with no extra NaCl. Ionic strength dependence like this is typically a marker of outer sphere adsorption as the background electrolyte can competitively adsorb in place of the citrate [57]. As the pH increased, the charge on the hematite surface became less positive resulting in a lessening of the ionic strength dependence and at ca. pH 8 very little change in the adsorption of citrate was observed. Above the pH_{pzc} approximately 20% of the maximum amount of citrate was still adsorbed (Fig. 1). At this pH, both citrate and hematite were negatively charged making the formation of electrostatically bound complexes unlikely, although not out of the question. For example, Hwang et al. [35] reported phthalic acid adsorbing predominantly as an outer sphere species on hematite at pH approaching and above the pH_{pzc}. Persson et al. [58] found a similar pattern for phthalate on goethite where the phthalate adsorbed in an inner-sphere manner at low pH and outer-sphere at high pH. Likewise, Lackovic et al. [32] found that citrate adsorbed on goethite predominantly as an inner-sphere complex, however, an outer-sphere complex was needed at high pH to adequately explain the adsorption behavior.

3.2. FTIR spectroscopy

3.2.1. Reference spectra

Infrared spectra of aqueous citrate and ferric citrate were collected across a range of pH values for use as reference spectra (Fig. 3). The citrate spectra show a dominant peak at ~1720 cm^{-1} at low pH, resulting from the carbonyl stretch ($\nu_{C=O}$) associated with protonated carboxyl groups, which was reduced in intensity with increasing pH as the carboxyl groups deprotonated until it was absent at a pH of 5.5. As the intensity of the carbonyl peak waned with increasing pH, peaks at 1570 cm^{-1} and 1390 cm^{-1} appeared and correspondingly grew in intensity. These two features represent the asymmetric (ν_{as}) and symmetric (ν_s) carbon – oxygen stretches of carboxylate groups, respectively [32,33]. The peak at ~1226 cm^{-1} was also dominant at low pH and with increasing pH it decreased in conjunction with the carbonyl stretch suggesting it originated from protonated carboxylic acid groups. DFT calculations show this feature was related to C—O—H bending (δ_{C-OH}) of the carboxylic acid groups. The feature centered at about 1280 cm^{-1} can be resolved into three individual peaks at 1257, 1280 and 1296 cm^{-1} and from DFT analyses the peak at ~1280 cm^{-1} was related to the C—O—H bending of the hydroxyl group while the two peaks surrounding it resulted from C—H rocking motions from the citrate skeleton. From these simulations, the shoulder in the symmetric stretch at ~1435 cm^{-1} resulted from both the C—H rocking motions on the citrate skeleton as well as the C—O—H bending motion of the hydroxyl group.

Table 1
Constants used for triple layer model fitting. All values taken from Hwang and Lenhart [24] aside from the results of the best model fit of 1000 μM citrate to the LSA hematite (Eqs. (5)–(7)). Values given as logs of equilibrium constants.

	N_S (sites/nm^2)	pH_{pzc}	C_1 (F/m^2)	C_2 (F/m^2)	SSA (m^2/g)
LSA	2.3	9.05	0.92	0.2	35
HSA	2.3	9.17	0.59	0.2	99
Eq			Log K	LSA	HSA
1	>FeOH => > FeO^- + H^+		K_{a1}	6.42	6.20
2	>FeOH + H^+ => > $FeOH_2^+$		K_{a2}	−11.68	−11.92
3	>FeOH + Na^+ => > FeO^-—Na^+ + H^+		K_{cation}	−8.58	−8.32
4	>FeOH + Cl^- + H^+ => > $FeOH_2^+$—Cl^-		K_{anion}	9.47	9.90
5	$(>FeOH)_2$ + H_3Cit => $(>FeOH_2^+)_2$—$HCit^{2-}$		K_{OS1}	20.23	20.68
6	$(>FeOH)_2$ + H_3Cit => $(>FeOH_2^+)_2$—Cit^{3-} + H^+		K_{OS2}	13.70	14.15
7	$(>FeOH)_2$ + H_3Cit => > $Fe_2H_{-1}Cit^{2-}$ + $2H_2O$ + $2H^+$		K_{IS}	−2.23	−1.78

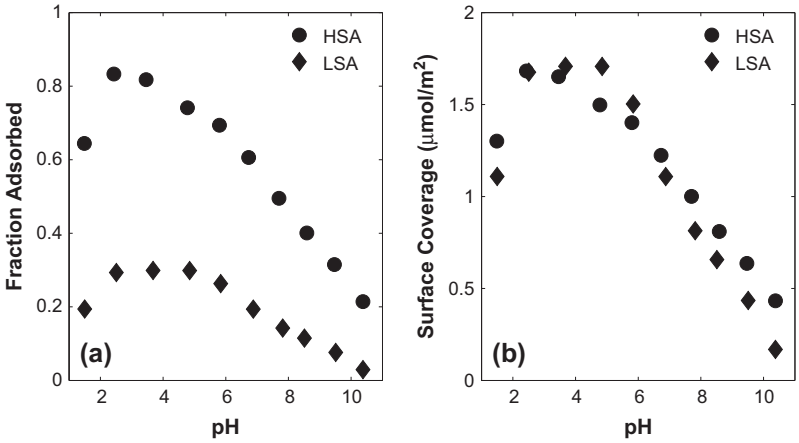

Fig. 1. Adsorption envelope for citrate (1000 μM) adsorbed onto LSA and HSA hematite at saturated conditions presented as (a) fraction adsorbed and (b) surface coverage.

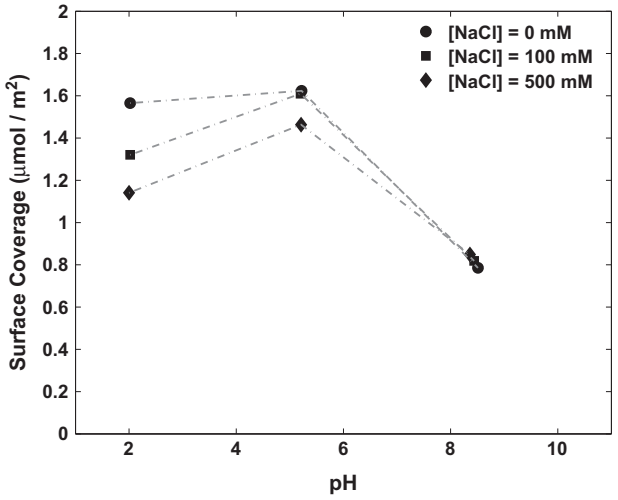

Fig. 2. Surface coverage of adsorbed citrate on the LSA hematite as a function of pH at 3 different NaCl concentrations.

The spectrum for ferric citrate was largely similar to that for citrate at pH above 3.5 with the symmetric, asymmetric, and carbonyl stretches present at similar locations (Fig. 3). Differences exist, however. For example, the decreased intensity of the carbonyl stretch relative to the C—O and C—O asymmetric stretches indicated the carboxylic acid groups deprotonated at a lower pH in the presence of iron. The feature at 1280 cm^{-1} associated with the C—O—H hydroxyl bending motion was also clearly reduced in the presence of bound ferric iron. Finally, the two peaks bracketing the 1280 cm^{-1} peak, which were related to C—H rocking, were more clearly defined peaks as opposed to the shoulders observed in the citric acid spectra. The changes in the spectra at ~1280 cm^{-1} presumably reflect the hydroxyl group deprotonating and taking an active role in binding ferric iron in the complex. The deprotonation of the hydroxyl group was consistent with previously reported structures of ferric citrate crystals precipitated from circumneutral pH solutions where citrate was present in excess of iron [14,59]. Similar ferric structures have also been observed in solution over a range of pH values with the hydroxyl group deprotonating more as the pH increases [60].

3.2.2. Adsorbed citrate spectra

Similar to spectra for aqueous citrate and ferric citrate, those for citrate adsorbed on the LSA hematite were dominated by carbonyl, C—O asymmetric and C—O symmetric stretches across a range of pH values (Fig. 4). However, there were several subtle differences between the aqueous and adsorbed citrate that provide insight into the structure of the adsorbed complex. To begin, although the dominant peaks show little shift in position they do exhibit an increase in peak width. The similarity in the position of the major peaks between the reference solution phase spectra and those for adsorbed citrate suggests citrate was electrostatically bound as an outer sphere complex [61,62]. This was consistent with the reduction in citrate adsorption at low pH with increasing ionic strength (Fig. 2). According to Roddick-Lanzilotta and McQuillan [62], broadening of IR peaks, with no change in position, results from the formation of complexes where the carboxyl groups' conformation remain similar to that formed in the aqueous state, such as outer sphere complexes or a bridging multi-dentate inner-sphere complex. The presence of the symmetric and asymmetric C—O stretches in the pH 2.5 adsorbed citrate spectrum indicates citrate was partially deprotonated at the surface since these features were not present in the corresponding aqueous-phase spectrum (Fig. 1). This was consistent with the expected shift in the interfacial pH towards the pH_{pzc} [63]. Using the diffuse layer model, Dzombak and Morel [56] demonstrated the pH of a 100 mM 1:1 electrolyte solution will shift from 2.5 in the bulk to around 5 near the surface. A similar shift in our system would take citrate from a fully protonated state in the bulk solution to a mixture of roughly 67% doubly protonated and 25% singly protonated citrate near the surface.

Evidence for the presence of an additional complex was manifest in the spectra when the concentration of citrate was varied (Fig. 5). At a total citrate concentration of 62.5 μM at pH 3, nearly 100% of the total citrate was adsorbed. The resulting spectrum shows no carbonyl peak at 1720 cm^{-1}, however the ν_{asC-O} and ν_{sC-O} were present and had peak heights of roughly 30% and 50% those at the maximum citrate concentration of 500 μM. As the citrate concentration was increased, the carbonyl peak gradually appears suggesting the presence of an additional protonated complex, likely outer-sphere. The absence of a carbonyl peak at low citrate concentrations likely reflects at low surface coverages that citrate preferentially adsorbs in this deprotonated manner to a limited number of sites. Increasing surface coverage consequently results in the formation of additional outer-sphere complexes that were protonated. Evidence of such a preferential adsorption mode of citrate at specific hematite surface sites was supported by the observation of Cornell and Schwertmann [20] that adding citrate to an Fe(III) solution during hematite synthesis causes the hematite to grow along the (001) face due to the specific adsorption of citrate to the (110) and (104) surfaces. The (001) face consists

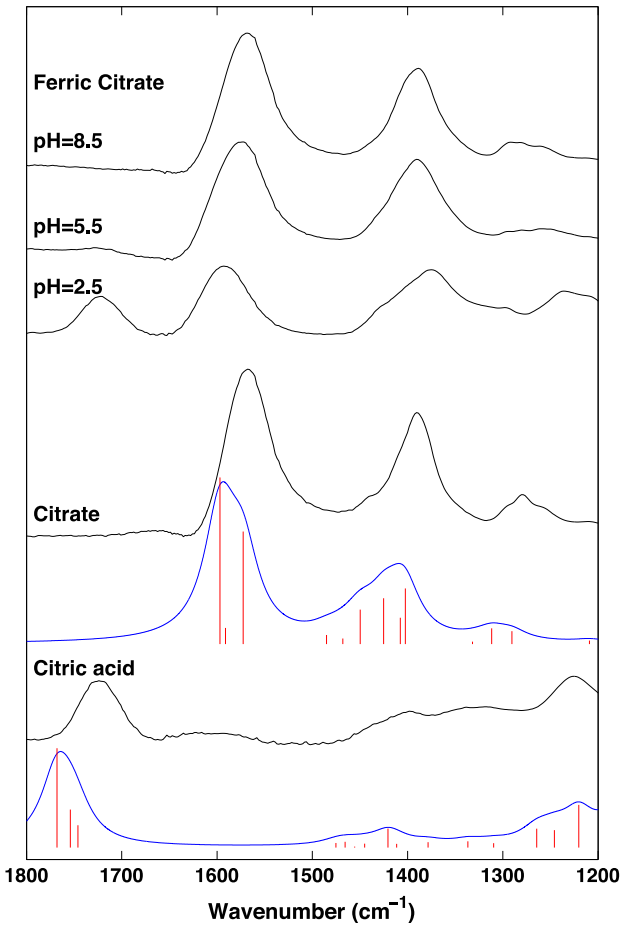

Fig. 3. Reference spectra used for comparison to adsorbed citrate spectra. The ferric citrate spectra at 3 pH values represent models for inner-sphere complexation. Additional experimental spectra (top, black) are presented for fully protonated citric acid (pH 2.5) and fully deprotonated citrate (pH 9.5). Corresponding theoretical spectra are also presented (blue, bottom) where the vertical lines (red) represent the individual absorbance frequencies from the DFT calculation. (For interpretation of the references to color in this figure legend, the reader is referred to the web version of this article.)

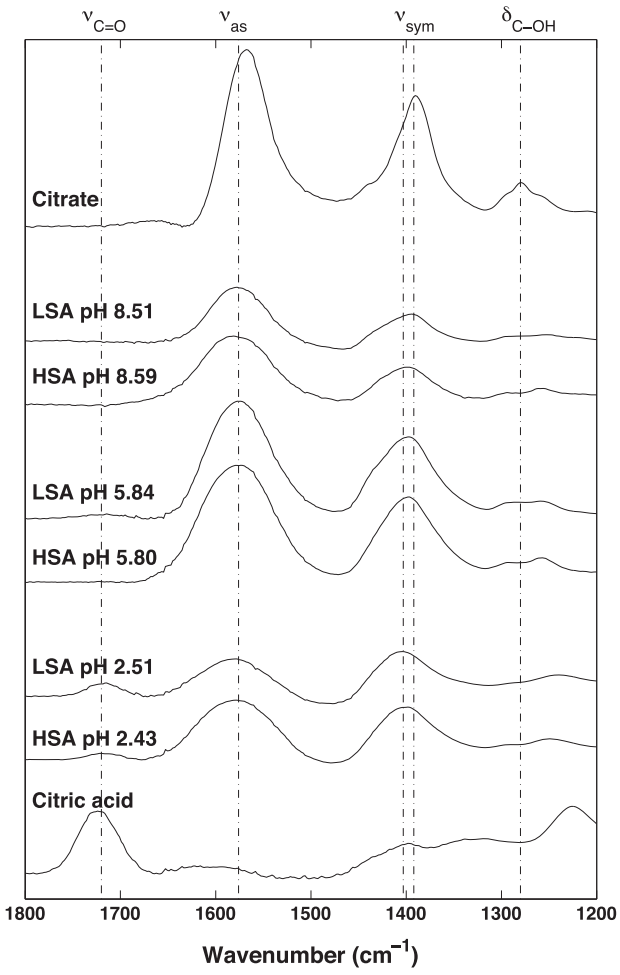

Fig. 4. Spectra for adsorbed citrate on LSA and HSA hematite at given pH values (1 mM citrate).

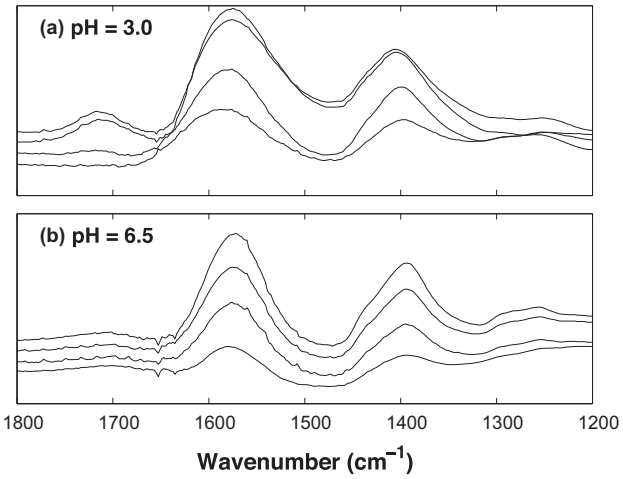

Fig. 5. FTIR spectra of citrate adsorbed on LSA hematite at (a) pH 3.0 and (b) 6.5. The citrate concentrations for the spectra from bottom to top for both pH values were 62.5, 125, 250, 500 μM.

of only doubly coordinated hydroxyl groups and it is neutrally charged at environmentally relevant pH values [64]. The (1 1 0) and (1 0 4) faces consist of singly, doubly and triply coordinated hydroxyl groups, which appear to be preferential for citrate adsorption [64]. The outer sphere complex was evident at elevated pH values as well based on the peak broadening and lack of shift in peak position compared to the aqueous citrate spectra (see Fig. 4).

At pH 6, there was also evidence of an inner-sphere structure in the feature at 1280 cm^{-1} which arises from the C—O—H bending motion. This feature was nearly absent at 62.5 μM citrate, indicating that either the hydroxyl deprotonates and takes an active role in the adsorption process as seems likely when complexing ferric iron [14,59] (see Fig. 3) or due to its proximity to the surface it was constrained and prevented from moving freely. Both options require direct binding to the surface. As the concentration was increased, this feature becomes more obvious; however, at maximum surface coverage it was not as prominent as it was in the aqueous citrate spectra (see Fig. 3).

The high surface area hematite spectra (Fig. 4) show a similar pattern as the LSA hematite. The biggest difference between the two was in the carbonyl stretching region at low pH where the HSA spectra had a much smaller carbonyl stretch. The ν_{asC-O} and ν_{sC-O} features for both HSA and LSA were comparable. The carbonyl stretch in the HSA spectra was nearly gone by pH 3.46 whereas in the LSA spectra it persists until pH 5.5. As the variable citrate concentration LSA spectra showed, citrate has a preferential fully deprotonated inner sphere adsorption mode that dominates at lower citrate concentrations before citrate begins adsorbing in an outer-sphere manner at higher concentrations. The subdued

Table 2
DFT assignments of simulated peaks for citrate and citric acid.

Citric acid		$Citrate^{3-}$	
Wavenumber	Assignment	Wavenumber	Assignment
1745.97, 1753.95, 1768.01	$\nu_{C=O}$	1572.50, 1591.06, 1596.98	ν_{asym}
1420.56, 1444.98	δ_{CH2}, δ_{COH}	1449.69	δ_{COH}
1175.51, 1220.23, 1245.76	δ_{CH2}, δ_{COH}	1402.30, 1407.60, 1425.07	ν_{sym}
		1290.40, 1331.70	δ_{CH2}
		1311.75	δ_{CH2}, δ_{COH}

Table 3
Experimental and theoretical symmetric and asymmetric stretch peak locations. The protonated mononuclear tridentate structure did not exhibit either a symmetric or asymmetric stretch. Structures for theoretical complexes are show in Fig. S2.

System	pH	$\nu_{C=O}$	ν_{as}	ν_{sym}
Citrate	1.5	1724.9		1398.7
	3.5	1723.2	1578.8	1397.5
	5.6	1725.9	1569.7	1390.3
	8.7		1567.3	1390.1
FeCit	3.5		1590	1385.5
	5.5		1577.2	1389.8
	8.5		1567.3	1388.9
10 nm Hem	2.4	1720.4	1578.7	1398.3
	5.8		1573.3	1397.3
	9.5		1579.5	1397.2
50 nm Hem	2.5	1715.2	1579.1	1403.4
	5.8	1714.3	1576.8	1397.3
	9.5		1577.6	1394.9
Theoretical				
IS-mononuclear		1754.4	1641.7	1370.9
IS mononuclear deprotonated			1601.9	1302.7
IS bidentate		1748.5	1590.8	1414.4
IS bidentate deprotonated			1597.3	1436.9
IS bidentate hydroxyl		1664.4	1581.1	1371.4
IS bidentate hydroxyl DP			1583.9	1398.3
OS		1726.2	1606.8	1410.0
OS deprotonated			1576.1	1411.7

carbonyl stretch relative to that in the LSA spectra suggest that the HSA hematite had a higher percentage of sites that favor inner-sphere complex formation. Madden et al. [26] report that high surface area hematite particles prepared using similar methods show an increased affinity with copper(II) ions when compared to a lower surface area hematite. Madden et al. [26] attribute this to an increase in the number of surface sites on the higher surface area hematite that suit the distorted octahedron binding environment that Cu(II) prefers. The differences in citrate adsorption observed for LSA and HSA hematite could reflect similar differences in available surface sites.

3.3. Computational modeling

The computed spectra for citric acid (H_3Cit) and citrate (Cit^{-3}) (Fig. 3) did not require a scaling factor in order to match the experimental symmetric and asymmetric peak locations, therefore no scaling factor was applied to either the aqueous or the adsorbed citrate results. Explicit water molecules were required, however, as their inclusion resulted in the computed spectra peak position and intensity being closer to those in the aqueous citrate experimental spectra (comparison shown in Fig. S3). The major area of improvement was observed for the C—O—H bending of the hydroxyl group, which in the absence of explicit water molecules had a calculated intensity equal to that for the C—O symmetric stretch. Experimentally, however, the C—O—H bending feature appears as a shoulder to the symmetric C—O stretch at $\sim$1443 cm^{-1} in the experimental spectra (Fig. 3).

Proposed structures for adsorbed citrate were informed by the batch adsorption and spectroscopic data. The FTIR results suggest outer-sphere or binuclear bidentate inner-sphere complexation modes and thus these were the initial, though not sole, focus of the computational simulations. Both singly protonated and fully deprotonated conformations were simulated as the appearance of the carbonyl stretch in the pH 3 adsorbed citrate spectra at $\sim$1720 cm^{-1} with increasing surface coverage (Fig. 5) suggested both could exist. The peak locations of the experimental and theoretical spectra are summarized in Tables 2 and 3 and plotted in comparison to one another in Fig. S4. Select theoretical spectra are shown in Fig. 6 (structures shown in Fig. S2) using a Lorentzian distribution with the full width at half height of 20 cm^{-1} for all peaks [65]. As the signal from the water and hematite were subtracted from the experimental FTIR spectra by the subtraction of standards, the features arising primarily from the iron cluster and explicit water molecules were excluded from the computed spectra using Gaussian 09.

The mononuclear bidentate complex (see CT-MN in Fig. S2) structure had citrate bound to a single iron atom by the central carboxyl (the carboxyl group attached to the central carbon on the citrate backbone, adjacent to the hydroxyl group) and one terminal carboxyl group (one of the two on either end of the molecule). This arrangement does not match the experimental data well. The

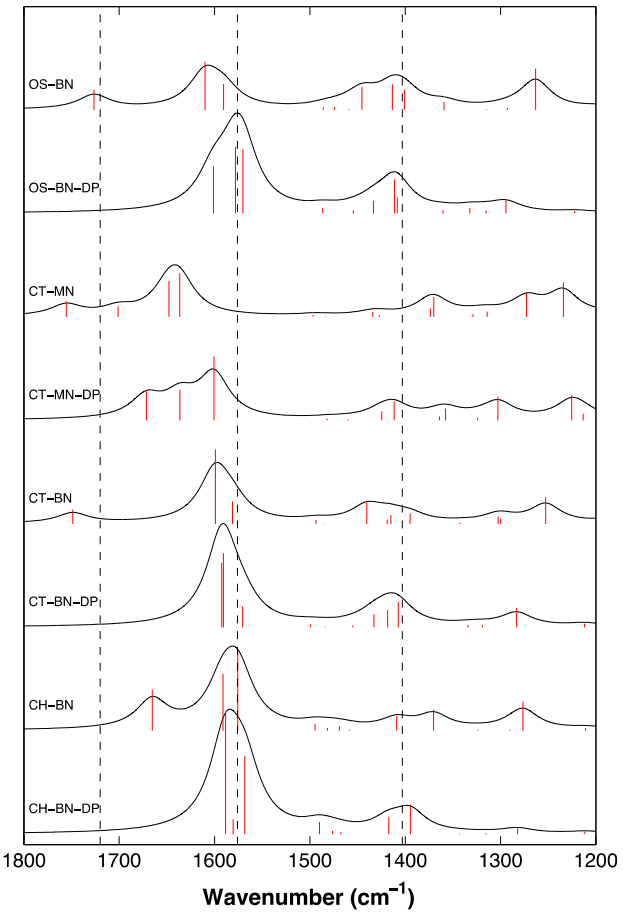

Fig. 6. Selected theoretical infrared spectra for adsorbed citrate structures visualized with a Lorentzian distribution with a 20 cm^{-1} FWHM. The short red vertical lines represent the absorption energies. The dashed vertical lines reflect the peak locations for the experimental results of the low surface area hematite at mildly acidic pH (OS = outersphere, MN = mononuclear, BN = binuclear, DP = deprotonated, CT = central and terminal carboxyl bonding, CH = central and hydroxyl bonding). The optimized structures are shown in supporting information (Fig. S2). (For interpretation of the references to color in this figure legend, the reader is referred to the web version of this article.)

peaks representing ν_{as} and ν_s were further apart than in the experimental data and the ν_{as} and ν_s were split into several distinct peaks. Based on this, the likelihood that mononuclear complexes formed at the hematite surface appears low.

The location of the carbonyl stretch, which was only present in the experimental spectra below pH 5.5, was not correct in any of the inner-sphere theoretical spectra. The bidentate structure involving the deprotonated hydroxyl group (CH-BN in Fig. S2) produced a theoretical carbonyl stretch at 1665 cm^{-1}, well below the LSA experimental value of 1720 cm^{-1}, while the central and terminal carboxyl bound model (CT-BN in Fig. S2) errs the other way at 1749 cm^{-1}. The outer-sphere structure (OS-BN in Fig. S2) produced a carbonyl stretch that was much closer at 1726 cm^{-1}. This, along with the influence of ionic strength on adsorption at low pH (see Fig. 1) indicates the protonated citrate complex was likely an outer-sphere complex.

The fully deprotonated bidentate model that included a deprotonated hydroxyl group interacting with the iron cluster and the outer-sphere models were the atomic configurations that most accurately matched the experimentally determined symmetric and asymmetric C—O stretches. The ν_s of the protonated outer-sphere complex was at 1411 cm^{-1} (1410 cm^{-1} for the deprotonated OS complex) and for the inner-sphere complex with the deprotonated hydroxyl group it was at 1398 cm^{-1}. There was a minor shift in the position of ν_s of adsorbed citrate in the experimental LSA spectra from 1403 to 1394 cm^{-1} as pH increased, likely related to the sequential deprotonation of the citrate. This shift was not seen in the HSA hematite spectra where the ν_s for adsorbed citrate remained at ~1398 cm^{-1} over the entire range of pH tested (see Fig. 4), indicating that citrate adsorbed to HSA hematite was fully deprotonated at a lower pH and possibly indicating inner-sphere binding was more dominant than outer-sphere binding. This shift in peak location was seen as an additional shoulder in the data presented by Lindegren et al. [33] for citrate on goethite and it was attributed to conformational changes in the adsorbed citrate.

3.4. Surface complexation modeling

Surface complexation modeling was performed to further test the structures determined from the match of the theoretical spectra to the experimental spectra. The triple layer model was used with published constants for surface protolysis and electrolyte binding for both sizes of hematite [24] with citric acid solution chemistry taken from Stumm and Morgan [17] and Silva et. al. [18] (see Table S1). The site density, N_S, was set at 2.3 sites/nm^2 as fitting the data to a Langmuir isotherm yields a Γ_{max} of 1.83 μmol/m^2 or 2.2 sites/nm^2, very close to the recommended and commonly used 2.3 sites/nm^2 [66]. The stoichiometry shown in Eqs. (5)–(7) of Table 3 represent the best fitting outer- and inner-sphere species being considered. Fits to these reactions were conducted for a citrate concentration of 1000 μM on the LSA hematite, which produces a saturated condition on the hematite surface. These constants were then fixed and the model was tested against different solution condition data sets. The binuclear stoichiometry was used as it was the most likely arrangement resulting from the FTIR analysis and molecular modeling and was also consistent with studies of citrate on goethite [33] and corundum [30]. Two outer-sphere complexes were tested, a singly protonated species and a fully deprotonated species, both bound to two fully protonated $FeOH_2$ sites (see Fig. S5). The entire charge for the outer-sphere citrate complex was placed in the beta layer. Additional simulations that distributed the charge to different planes did not result in marked improvements in model fits. The inner-sphere complex included a completely deprotonated citrate molecule, with a charge of −4 (see Fig. S5). The reaction was modeled as a ligand exchange reaction with all of the complex charge directly at the surface. As was done for the outer-sphere species, simulations placing the charge of the inner-sphere species at different planes did not improve the model.

Fits were performed using just the outer-sphere complexes or with a combination of the outer- and inner-sphere surface complexes. The WSOS/DF for the outer-sphere only model on the LSA hematite was 1.92. Including the inner-sphere complex only reduced it slightly to a value of 1.33, but were more consistent with the spectroscopic and molecular modeling results. Simulations with this dual-mode model indicated the singly protonated outer-sphere complex was dominant, accounting for approximately 90% of the adsorption at low pH (see Fig. 7a). This continued as the pH was raised until the deprotonated outer-sphere complex became dominant at a pH of 8.5. This description of the system appears to vary slightly from the adsorbed citrate FTIR data in that the carbonyl peak at 1720 cm^{-1}, the indicator of protonated carboxyl group, disappears above a pH of 5.5 (see Fig. 4). At this pH, the SCM model indicated the singly protonated outer-sphere citrate represented 90% of the total adsorbed citrate (Fig. 7a). Although this pH was below the third pK_a for citric acid, where over half of the citrate was present in the singly protonated state, the carbonyl peak was only slightly visible in the aqueous citrate IR

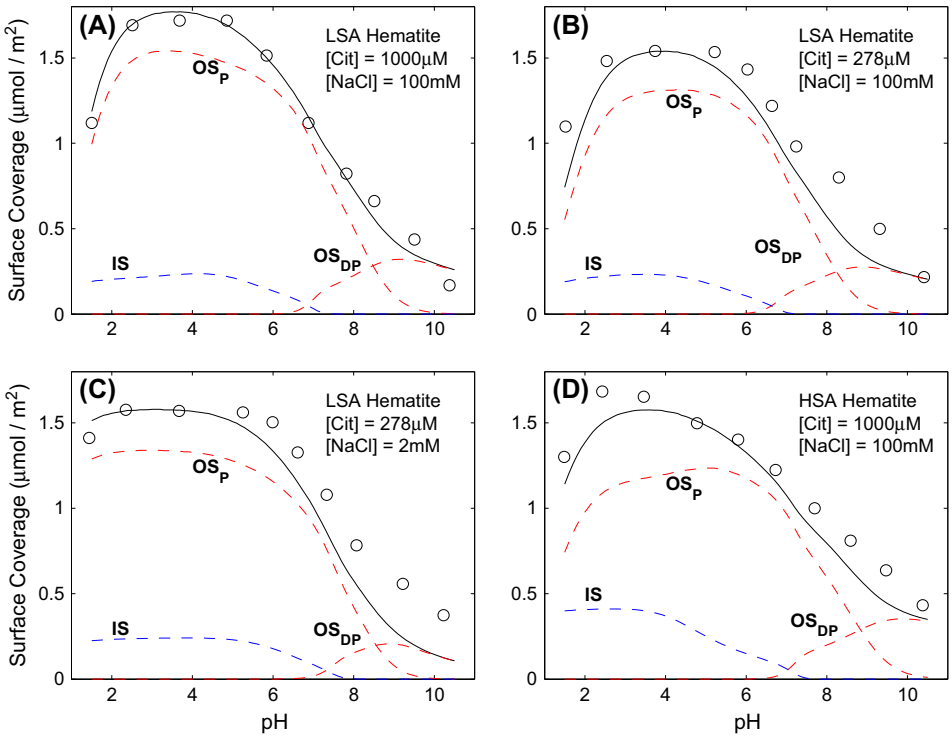

Fig. 7. Results of surface complexation modeling using one inner-sphere (IS), one singly protonated outer-sphere (OS_P) and one deprotonated outer-sphere (OS_{DP}) complex as described in Eqs. (5)–(7) of Table 1. Individual species are shown with dashed lines and the total adsorption with a solid line. Equilibrium constants were determined from the data in plot A and applied to data collected at other solution conditions (B–D).

spectrum (Fig. 3). Thus, while the SCM probably overestimates the singly protonated OS species, it was not a completely unreasonable fit as the protonated species can exist in significant concentrations with only a small carbonyl peak visible in the spectrum. There is precedence for a slight discrimination between the FTIR analysis and SCM fitting. Lackovic et al. [32]. also paired FTIR and SCM in investigating citrate on goethite and also had a singly protonated complex comprising the majority of the adsorbed species and existing well beyond the final pK_a of citrate. Hwang et al. [35] used FTIR to determine phthalate forms two inner sphere and one outer-sphere complexes on hematite, all deprotonated. The SCM fits following the FTIR analysis were accomplished using only one inner-sphere and one outer-sphere complexes, all deprotonated [38].

When these three adsorption reactions and related equilibrium constants were applied to data from a solution with 278 μM citrate, the quality of fit decreased (WSOS/DV = 37.4). At this citrate concentration, which results in slightly less than full surface coverage, the inclusion of the inner-sphere complex becomes more important and at low pH it accounted for 25% of the total adsorption (Fig. 7b). This was in agreement with the idea that at low pH the inner-sphere complex forms preferentially to a limited number of higher-affinity sites and as the citrate concentration increased and these sites were saturated the formation of outer-sphere complexes became important. At a lower electrolyte concentration (2 mM NaCl), the model prediction to the data produced a WSOS/DF value of 59.2 as the model fit the data well at low pH, but failed to capture the adsorption accurately at high pH values (Fig. 7c). This may be due to the presence of an additional inner-sphere complex that was not accounted for in the model. The inclusion of an additional inner-sphere complex would be consistent with the lack of change in the amount of citrate adsorbed at high pH as the ionic strength was varied (see Fig. 2). It has been suggested that citrate forms an inner-sphere complex on goethite [33] and corundum [30] in the slightly basic pH range and it was possible that is also the case on hematite, however, including an extra complex to our SCM model did not produce improved fits. In keeping with the proposed dominance of the outer-sphere complexes, the model predicts that lowering the ionic strength will cause an increase in the abundance of the outer-sphere complex, especially at low pH where the OS complex is increased from 0.55 μM at 100 mM NaCl to 1.29 μM at 2 mM NaCl.

Sverjensky [67,68], proposed the following method for adjusting equilibrium constants to account for variations in surface area that result when varying particle size:

$$\text{Log } K_\theta = \text{Log } K_0 \; N_S A_S / N_\# A_\#$$

where N_S is the site density for the sample, A_S is the specific surface area of the sample and K_θ is the equilibrium constant for the sample. $N_\#$, $A_\#$, and K_0 are the same values for the hypothetical standard state. In addition to using a different equilibrium constant for the HSA hematite, a new inner-layer capacitance, C_1, also provided by Hwang and Lenhart [24], must be used as C_1 has an inversely proportional relationship with specific surface area [24]. Using the LSA hematite with $N_\#$ set to 2.3 sites/nm^2 to determine the equilibrium constants for the HSA sample and the parameter values from Hwang and Lenhart [24] summarized in Table 1, resulted in a model predicted WSOS/DF of 15.3 for the dual-mode model applied to the HSA hematite with 1000 μM citrate (Fig. 7d). As expected for the smaller hematite, the lower C_1 increased the importance of the inner-sphere complex as a smaller C_1 physically implies a greater distance between the surface and the beta plane [69]. The increase in inner-sphere complexation as the particle size was reduced was consistent with both the spectroscopic data presented here and previously reported dual-mode model fits of phthalic acid adsorption on hematite [38]. However, it contradicts the model proposed by Lackovic et al. [32] for citrate on goethite using an extended constant capacitance model. In their model, a singly protonated mononuclear monodentate inner-sphere complex dominates, accounting for nearly all adsorption below pH 7.7. Above pH 7.7, a deprotonated outer-sphere complex also arises. Although the

model of Lackovic et al. [32] is very different from ours, it also failed to accurately match adsorption data at high pH values. This suggests an additional species that was not accounted for in our modeling effort, or those previously conducted, might exist. Thus, additional effort is needed to determine the nature of the additional adsorption mode at high pH.

4. Conclusion

Explicitly defining details of the adsorption of organic molecules like citrate on iron oxides is not a straightforward problem. For goethite, many methods have been used to study citrate adsorption, but as of yet a consensus on the exact adsorption mechanism does not exist. The four methods of determining the structure of citrate on the hematite surface used in this study all point to outer-sphere complexes dominating the adsorption of citrate on hematite surfaces across all pH values. These complexes differ on the basis of protonation state, with the outer-spherically bound citrate molecule changing from singly protonated to a fully deprotonated complex at a pH of approximately 5.5–6.5. Supplementing these species was a fully deprotonated binuclear bidentate inner-sphere complex. The inner-sphere complex formed to a greater extent at lower citrate concentrations while the outer-sphere complex was formed across all citrate concentrations studied. This reflects the limited amount of inner-sphere sites relative to those available for the electrostatically held citrate. The inner-sphere mode appears to be slightly more significant in the HSA hematite, indicating the proportion of the sites to which citrate adsorbs directly does not change in exact proportion with the overall hematite surface area. Testing a broader range of hematite particle sizes and morphologies is necessary to arrive at a definitive conclusion on the impact of particle dependent reactivity.

Acknowledgments

We would like to thank the National Science Foundation under Grant No. 0954991 for providing funding for this research. We also acknowledge the Ohio Supercomputer Center for use of their computational resources.

Appendix A. Supplementary material

Supplementary data associated with this article can be found, in the online version, at http://dx.doi.org/10.1016/j.jcis.2015.08.028.

References

[1] K. Axe, M. Vejgarden, P. Persson, An ATR-FTIR spectroscopic study of the competitive adsorption between oxalate and malonate at the water–goethite interface, J. Colloid Interface Sci. 294 (1) (2006) 31–37.
[2] B. Zinder, G. Furrer, W. Stumm, The coordination chemistry of weathering: II. Dissolution of Fe (III) oxides, Geochim. Cosmochim. Acta 50 (9) (1986) 1861–1869.
[3] J.A. Davis, Adsorption of natural dissolved organic matter at the oxide/water interface, Geochim. Cosmochim. Acta 46 (11) (1982) 2381–2393.
[4] M. Hassellov, F. von der Kammer, Iron oxides as geochemical nanovectors for metal transport in soil-river systems, Elements 4 (6) (2008) 401–406.
[5] J.A. Davis, J.O. Leckie, Effect of adsorbed complexing ligands on trace metal uptake by hydrous oxides, Environ. Sci. Technol. 12 (12) (1978) 1309–1315.
[6] J.M. Kaste, B.C. Bostick, A.J. Friedland, A.W. Schroth, T.G. Siccama, Fate and speciation of gasoline-derived lead in organic horizons of the northeastern USA, Soil Sci. Soc. Am. J. 70 (5) (2006) 1688.
[7] J.F. McCarthy, J.M. Zachara, Subsurface transport of contaminants, Environ. Sci. Technol. 23 (5) (1989) 496–502.
[8] N. Teutsch, Y. Erel, L. Halicz, A. Banin, Distribution of natural and anthropogenic lead in Mediterranean soils, Geochim. Cosmochim. Acta 65 (17) (2001) 2853–2864.
[9] S.E. Cabaniss, Q. Zhou, P.A. Maurice, Y.-P. Chin, G.R. Aiken, A log-normal distribution model for the molecular weight of aquatic fulvic acids, Environ. Sci. Technol. 34 (6) (2000) 1103–1109.
[10] J.J. Lenhart, S.E. Cabaniss, P. MacCarthy, B.D. Honeyman, Uranium (VI) complexation with citric, humic and fulvic acids, Radiochim. Acta 88 (6/2000) (2000) 345.
[11] K.H. Tan, Principles of Soil Chemistry, CRC Press, 2011.
[12] C.R. Evanko, D.A. Dzombak, Influence of structural features on sorption of NOM-analogue organic acids to goethite, Environ. Sci. Technol. 32 (19) (1998) 2846–2855.
[13] B.W. Strobel, Influence of vegetation on low-molecular-weight carboxylic acids in soil solution–a review, Geoderma 99 (3–4) (2001) 169–198.
[14] J. Pierre, I. Gautier-Luneau, Iron and citric acid: a fuzzy chemistry of ubiquitous biological relevance, BioMetals 13 (1) (2000) 91–96.
[15] R. Hell, U.W. Stephan, Iron uptake, trafficking and homeostasis in plants, Planta 216 (4) (2003) 541–551.
[16] P. Barone, D. Rosellini, P. LaFayette, J. Bouton, F. Veronesi, W. Parrott, Bacterial citrate synthase expression and soil aluminum tolerance in transgenic alfalfa, Plant Cell Rep 27 (5) (2008) 893–901.
[17] W. Stumm, J. Morgan, Aquatic Chemistry, third ed., Wiley, New York, 1996.
[18] A.M.N. Silva, X. Kong, R.C. Hider, Determination of the pKa value of the hydroxyl group in the α-hydroxycarboxylates citrate, malate and lactate by 13C NMR: implications for metal coordination in biological systems, BioMetals 22 (5) (2009) 771–778.
[19] M. Clausén, L.-O. Öhman, P. Persson, Spectroscopic studies of aqueous gallium (III) and aluminum(III) citrate complexes, J. Inorg. Biochem. 99 (3) (2005) 716–726.
[20] R.M. Cornell, U. Schwertmann, The Iron Oxides: Structure, Properties, Reactions, Occurrences and Uses, Wiley-VCH, 2003.
[21] J.G. Catalano, C. Park, P. Fenter, Z. Zhang, Simultaneous inner- and outer-sphere arsenate adsorption on corundum and hematite, Geochim. Cosmochim. Acta 72 (8) (2008) 1986–2004.
[22] J. Gimenez, M. Martinez, J. Depablo, M. Rovira, L. Duro, Arsenic sorption onto natural hematite, magnetite, and goethite, J. Hazard. Mater. 141 (3) (2007) 575–580.
[23] T. Hiemstra, W.H. Van Riemsdijk, Effect of different crystal faces on experimental interaction force and aggregation of hematite, Langmuir 15 (23) (1999) 8045–8051.
[24] Y.S. Hwang, J.J. Lenhart, The dependence of hematite site-occupancy standard state triple-layer model parameters on inner-layer capacitance, J. Colloid Interface Sci. 319 (1) (2008) 206–213.
[25] J.R. Rustad, E. Wasserman, A.R. Felmy, Molecular modeling of the surface charging of hematite: II. Optimal proton distribution and simulation of surface charge versus pH relationships, Surf. Sci. 424 (1) (1999) 28–35.
[26] A. Madden, M. Hochella, T. Luxton, Insights for size-dependent reactivity of hematite nanomineral surfaces through Cu^{2+} sorption, Geochim. Cosmochim. Acta 70 (16) (2006) 4095–4104.
[27] F. Gaboriaud, J.-J. Ehrhardt, Effects of different crystal faces on the surface charge of colloidal goethite (α-FeOOH) particles: an experimental and modeling study, Geochim. Cosmochim. Acta 67 (5) (2003) 967–983.
[28] Y. Zhang, N. Kallay, E. Matijevic, Interaction of metal hydrous oxides with chelating agents. 7. Hematite-oxalic acid and-citric acid systems, Langmuir 1 (2) (1985) 201–206.
[29] N. Kallay, E. Matijevic, Adsorption at solid/solution interfaces. 1. Interpretation of surface complexation of oxalic and citric acids with hematite, Langmuir 1 (2) (1985) 195–201.
[30] P.C. Hidber, T.J. Graule, L.J. Gauckler, Citric acid—a dispersant for aqueous alumina suspensions, J. Am. Ceram. Soc. 79 (7) (1996) 1857–1867.
[31] R. Cornell, P. Schindler, Infrared study of the adsorption of hydroxycarboxylic acids on a-FeOOH and amorphous Fe (III) hydroxide, Colloid Polym. Sci. 258 (10) (1980) 1171–1175.
[32] K. Lackovic, B.B. Johnson, M.J. Angove, J.D. Wells, Modeling the adsorption of citric acid onto Muloorina illite and related clay minerals, J. Colloid Interface Sci. 267 (1) (2003) 49–59.
[33] M. Lindegren, J.S. Loring, P. Persson, Molecular structures of citrate and tricarballylate adsorbed on α-FeOOH particles in aqueous suspensions, Langmuir 25 (18) (2009) 10639–10647.
[34] S. Yeasmin, B. Singh, R.S. Kookana, M. Farrell, D.L. Sparks, C.T. Johnston, Influence of mineral characteristics on the retention of low molecular weight organic compounds: a batch sorption–desorption and ATR-FTIR study, J. Colloid Interface Sci. 432 (2014) 246–257.
[35] Y.S. Hwang, J. Liu, J.J. Lenhart, C.M. Hadad, Surface complexes of phthalic acid at the hematite/water interface, J. Colloid Interface Sci. 307 (1) (2007) 124–134.
[36] E. Matijevic, P. Scheiner, Ferric hydrous oxide sols12: III. Preparation of uniform particles by hydrolysis of Fe (III)-chloride,-nitrate, and-perchlorate solutions, J. Colloid Interface Sci. 63 (3) (1978) 509–524.
[37] N. Penners, L. Koopal, Preparation and optical properties of homodisperse haematite hydrosols, Colloids Surfaces 19 (2–3) (1986) 337–349.
[38] Y.S. Hwang, J.J. Lenhart, Surface complexation modeling of dual-mode adsorption of organic acids: phthalic acid adsorption onto hematite, J. Colloid Interface Sci. 336 (1) (2009) 200–207.
[39] L.J. Criscenti, D.A. Sverjensky, The role of electrolyte anions (ClO_4^-, NO_3^-, and Cl^-) in divalent metal (M^{2+}) adsorption on oxide and hydroxide surfaces in salt solutions, Am. J. Sci. 299 (1999) 828–899.
[40] C.J. Dodge, A.J. Francis, Photodegradation of a ternary iron (III)-uranium (VI)-citric acid complex, Environ. Sci. Technol. 36 (9) (2002) 2094–2100.

[41] P. Borer, S.J. Hug, B. Sulzberger, S.M. Kraemer, R. Kretzschmar, Photolysis of citrate on the surface of lepidocrocite: an in situ attenuated total reflection infrared spectroscopy study, J. Phys. Chem. C 111 (28) (2007) 10560–10569.
[42] P. Persson, K. Axe, Adsorption of oxalate and malonate at the water-goethite interface. Molecular surface speciation from IR spectroscopy, Geochim. Cosmochim. Acta 69 (3) (2005) 541–552.
[43] J. Kubicki, L. Schroeter, M. Itoh, B. Nguyen, S. Apitz, Attenuated total reflectance Fourier-transform infrared spectroscopy of carboxylic acids adsorbed onto mineral surfaces, Geochim. Cosmochim. Acta 63 (18) (1999) 2709–2725.
[44] J.D. Kubicki, M.J. Itoh, L.M. Schroeter, S.E. Apitz, Bonding mechanisms of salicylic acid adsorbed onto illite clay: an ATR-FTIR and molecular orbital study, Environ. Sci. Technol. 31 (4) (1997) 1151–1156.
[45] R.M. Cornell, U. Schwertmann, The Iron Oxides: Structure, Properties, Reactions, Occurrence and Uses, second ed., Wiley - VCH Weinham, 2003.
[46] K.W. Paul, J.D. Kubicki, D.L. Sparks, Sulphate adsorption at the Fe (hydr) oxide–H_2O interface. Comparison of cluster and periodic slab DFT predictions, Eur. J. Soil Sci. 58 (4) (2007) 978–988.
[47] J. Kubicki, K. Kwon, K. Paul, D. Sparks, Surface complex structures modelled with quantum chemical calculations: carbonate, phosphate, sulphate, arsenate and arsenite, Eur. J. Soil Sci. 58 (4) (2007) 932–944.
[48] A.D. Becke, Density-functional thermochemistry. III. The role of exact exchange, J. Chem. Phys. 98 (7) (1993) 5648–5652.
[49] C. Lee, W. Yang, R.G. Parr, Development of the Colle-Salvetti correlation-energy formula into a functional of the electron density, Phys. Rev. B 37 (2) (1988) 785–789.
[50] P.J. Stephens, F.J. Devlin, C.F. Chabalowski, M.J. Frisch, Ab initio calculation of vibrational absorption and circular dichroism spectra using density functional force fields, J. Phys. Chem. 98 (45) (1994) 11623–11627.
[51] W.J. Hehre, L. Radom, P.v.R. Schleyer, J.A. Pople, Ab Initio Molecular Orbital Theory, vol. 67, Wiley, New York, 1986.
[52] J. Tomasi, B. Mennucci, R. Cammi, Quantum mechanical continuum solvation models, Chem. Rev. 105 (8) (2005) 2999–3094.
[53] M. Frisch, G. Trucks, H. Schlegel, G. Scuseria, M. Robb, J. Cheeseman, G. Scalmani, V. Barone, B. Mennucci, G. Petersson, Gaussian 09 Revision A. 1, Gaussian Inc., Wallingford CT, 2009.
[54] J.C. Westall, O.S.U.D.o. Chemistry, FITEQL: A Computer Program for Determination of Chemical Equilibrium Constants from Experimental Data, Department of Chemistry, Oregon State University, 1982.
[55] L.E. Katz, K.F. Hayes, Surface complexation modeling I. Strategy for modeling monomer complex formation at moderate surface coverage, J. Colloid Interface Sci. 170 (2) (1995) 477–490.
[56] D.A. Dzombak, F. Morel, Surface Complexation Modeling: Hydrous Ferric Oxide, Wiley-Interscience, 1990.
[57] M.B. McBride, A critique of diffuse double layer models applied to colloid and surface chemistry, Clays Clay Miner. 45 (4) (1997) 598–608.
[58] P. Persson, J. Nordin, J. Rosenqvist, L. Lövgren, L.-O. Öhman, S. Sjöberg, Comparison of the adsorption ofo-Phthalate on boehmite (γ-AlOOH), aged γ-Al_2O_3, and goethite (α-FeOOH), J. Colloid Interface Sci. 206 (1) (1998) 252–266.
[59] M. Matzapetakis, C.P. Raptopoulou, A. Tsohos, V. Papaefthymiou, N. Moon, A. Salifoglou, Synthesis, spectroscopic and structural characterization of the first mononuclear, water soluble iron citrate complex, (NH4)5Fe(C6H4O7) 2∑2H2O, J. Am. Chem. Soc. 120 (50) (1998) 13266–13267.
[60] P. Vukosav, M. Mlakar, V. Tomišić, Revision of iron(III)–citrate speciation in aqueous solution. Voltammetric and spectrophotometric studies, Anal. Chim. Acta 745 (2012) 85–91.
[61] K.D. Dobson, A.J. McQuillan, In situ infrared spectroscopic analysis of the adsorption of aliphatic carboxylic acids to TiO_2, ZrO_2, Al_2O_3, and Ta_2O_5 from aqueous solutions, Spectrochim. Acta Part A: Mol. Biomol. Spectrosc. 55 (7–8) (1999) 1395–1405.
[62] A.D. Roddick-Lanzilotta, A.J. McQuillan, An in situ infrared spectroscopic study of glutamic acid and of aspartic acid adsorbed on TiO2: implications for the biocompatibility of titanium, J. Colloid Interface Sci. 227 (1) (2000) 48–54.
[63] S.B. Johnson, T.H. Yoon, B.D. Kocar, G.E. Brown, Adsorption of organic matter at mineral/water interfaces. 2. Outer-sphere adsorption of maleate and implications for dissolution processes, Langmuir 20 (12) (2004) 4996–5006.
[64] V. Barron, J. Torrent, Surface hydroxyl configuration of various crystal faces of hematite and goethite, J. Colloid Interface Sci. 177 (2) (1996) 407–410.
[65] R.W. Kawiecki, F. Devlin, P.J. Stephens, R.D. Amos, N.C. Handy, Vibrational circular dichroism of propylene oxide, Chem. Phys. Lett. 145 (5) (1988) 411–417.
[66] J.A. Davis, D.B. Kent, Surface complexation modeling in aqueous geochemistry, Rev. Mineral. Geochem. 23 (1) (1990) 177–260.
[67] D.A. Sverjensky, Prediction of surface charge on oxides in salt solutions: revisions for 1:1 (M+L−) electrolytes, Geochim. Cosmochim. Acta 69 (2) (2005) 225–257.
[68] D.A. Sverjensky, Standard states for the activities of mineral surface sites and species, Geochim. Cosmochim. Acta 67 (1) (2003) 17–28.
[69] D.A. Sverjensky, Interpretation and prediction of triple-layer model capacitances and the structure of the oxide-electrolyte-water interface, Geochim. Cosmochim. Acta 65 (21) (2001) 3643–3655.